

Investigating the formation of the Cretaceous Western Interior Seaway using landscape evolution simulations

Ching Chang† and Lijun Liu

Department of Geology University of Illinois at Urbana-Champaign, Urbana, Illinois 61801, USA

ABSTRACT

Transient intraplate sedimentation like the widespread Late Cretaceous Western Interior Seaway, traditionally considered a flexural foreland basin of the Sevier orogeny, is now generally accepted to be a result of dynamic topography due to the viscous force from mantle downwelling. However, the relative contributions of flexural versus dynamic subsidence are poorly understood. Furthermore, both the detailed subsidence history and the underlying physical mechanisms remain largely unconstrained. Here, we considered both Sevier orogenic loading and three different dynamic topography models that correspond to different geodynamic configurations. We used forward landscape evolution simulations to investigate the surface manifestations of these tectonic scenarios on the regional sedimentation history. We found that surface processes alone are unable to explain Western Interior Seaway sedimentation in a purely orogenic loading system, and that sedimentation increases readily inland with the additional presence of dynamic subsidence. The findings suggest that dynamic subsidence was crucial to Western Interior Seaway formation and that the dominant control on sediment distribution in the Western Interior Seaway transitioned from flexural to dynamic subsidence during 90-84 Ma, coinciding with the proposed emplacement of the conjugate Shatsky oceanic plateau. Importantly, the sedimentation records require the underlying dynamic subsidence to have been landward migratory, which implies that the underlying mechanism was the regional-scale mantle downwelling induced by the sinking Farallon flat slab underneath the westwardmoving North American plate. The simulated landscape evolution also implies that prominent regional-scale Laramide uplift in the

Ching Chang http://orcid.org/0000-0001-5397-0076

†cchang57@illinois.edu.

GSA Bulletin;

western United States should have occurred no earlier than the latest Cretaceous.

INTRODUCTION

The tectonic mechanisms that cause formation of large-scale (>200 km) continental inundation and intraplate sedimentation (Heine et al., 2008) remain elusive. Since most of these basins are situated in tectonically stable continental interiors (Artyushkov, 1992; Milanovsky, 1992), pure crustal or lithospheric isostasy-driven subsidence is an implausible mechanism. Dynamic topography, i.e., the vertical surface motion induced by sublithospheric mantle flow (Braun, 2010; Flament et al., 2013; Liu, 2015), has been proposed as a major cause for these geologic events (Gurnis et al., 1998; Liu and Nummedal, 2004; Heine et al., 2008; Liu et al., 2008; Müller et al., 2016, 2018; Rubey et al., 2017). However, there is little consensus on the relative significance (compared to flexural or isostatic topography), the spatiotemporal evolution, and the underlying mechanism of dynamic topography. The Cretaceous Western Interior Seaway (Bond, 1976) in North America serves as an ideal example for further understanding this problem, where multiple published models of dynamic subsidence (Mitrovica et al., 1989; Gurnis, 1993; Liu et al., 2008; Müller et al., 2016, 2018; Rubey et al., 2017) provide a spectrum of possible scenarios of surface process evolution during formation of the Western Interior Seaway.

The Western Interior Seaway is geologically phenomenal in that a massive landmass, spanning from the Gulf of Mexico to the Arctic Sea and more than 2000 km in the east-west direction at maximum, was inundated, and marine sediments accumulated during the Late Cretaceous in western-middle North America (Robinson Roberts and Kirschbaum, 1995). Earlier studies have found that neither a base-level rise due to sea-level change nor foreland basin subsidence due to the Sevier orogeny was sufficient to explain the spatial extent of the Western Interior Seaway, and studies have suggested that dynamic topography, likely related to Farallon

slab subduction, caused the subsidence necessary to form the Western Interior Seaway (Bond, 1976; DeCelles, 2004). There is an abundance of recent literature on the presence of dynamic topography in the sedimentation history of the Western Interior Seaway (Mitrovica et al., 1989; Liu and Nummedal, 2004; Liu et al., 2005, 2008, 2014; Leary et al., 2015; Yonkee and Weil, 2015; Liu, 2015; Heller and Liu, 2016).

Recent efforts in estimating the amount and pattern of dynamic topography causing the Western Interior Seaway mostly have utilized stratigraphic profiles (Liu and Nummedal, 2004; Liu et al., 2011, 2014; Tufano and Pietras, 2017), theoretical calculations (Mitrovica et al., 1989), and geodynamic simulations (Liu et al., 2008; Spasojevic et al., 2009; Müller et al., 2016, 2018; Rubey et al., 2017). The dynamic topography below the Western Interior Seaway is also suggested to have been geographically migratory based on the tilted strata and migrating depocenter of Western Interior Seaway stratigraphy (Liu et al., 2011). A recent study using synthetic forward landscape evolution simulations affirmed the inference that only a migratory subsidence profile can lead to these characters of intracontinental basins (Chang and Liu, 2019).

However, a systematic investigation into the quantitative contributions of flexural (DeCelles, 2004; Painter and Carrapa, 2013; Leary et al., 2015) versus dynamic subsidence (Liu et al., 2008, 2011; Rubey et al., 2017; Müller et al., 2018) on the sedimentation history is lacking. There also a lack of comprehensive analyses on the sediment transport from source to sink during the Western Interior Seaway formation, such that the connection of surface processes to various subsidence mechanisms remains elusive. In addition, both the detailed subsidence history of the Western Interior Seaway and the underlying physical mechanisms remain largely unconstrained. Landscape evolution simulation can not only quantify the surface responses to different types of tectonic forcing, but it can also provide a comprehensive analysis on their respective significance. Therefore, simulating surface processes due to both flexural and

https://doi.org/10.1130/B35653.1; 10 figures; 1 table; 1 supplemental file.

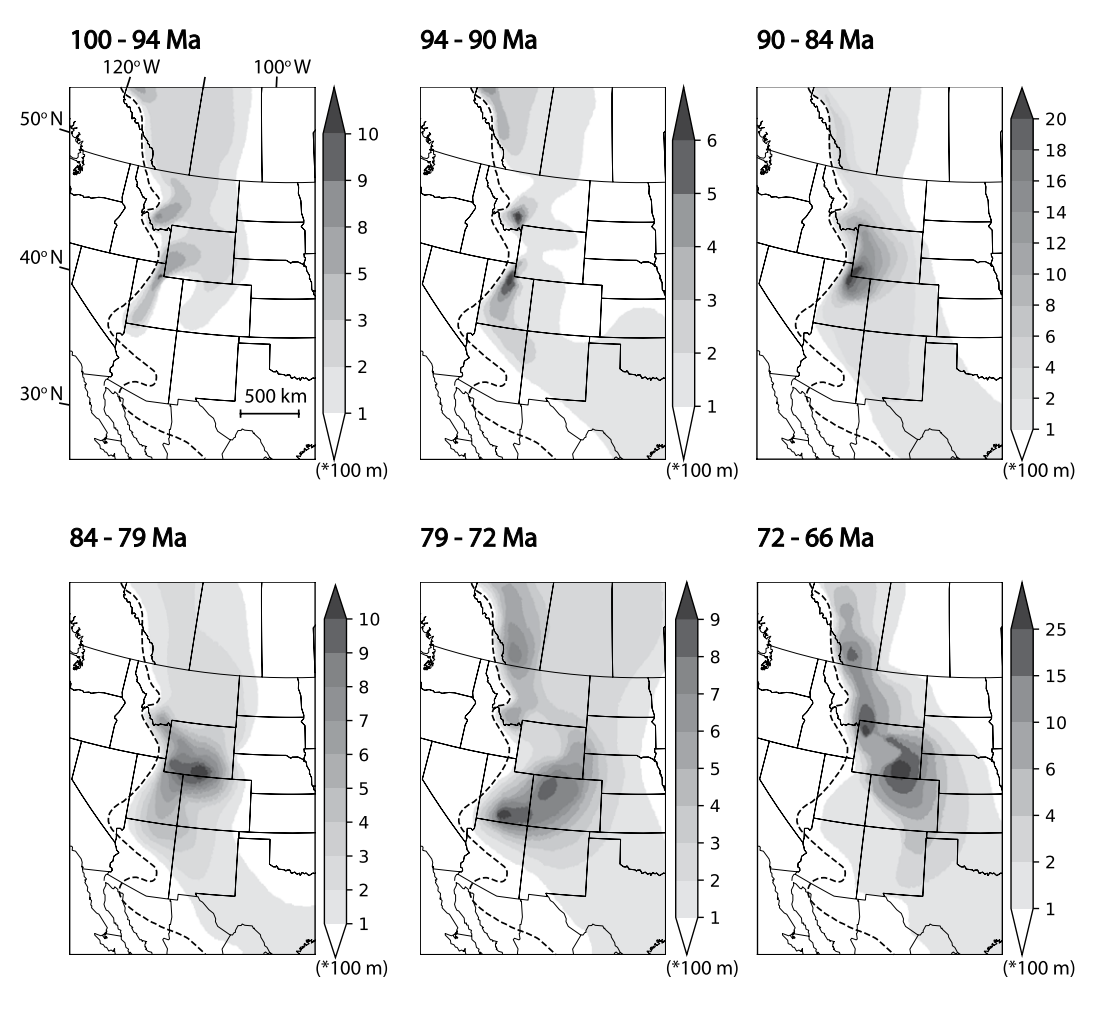


Figure 1. Observed Western Interior Seaway sedimentation patterns (adapted from Robinson Roberts and Kirschbaum, 1995) in western-middle North America for six episodes over the Late Cretaceous. The black dashed line outlines the western edge of the Western Interior Seaway.

dynamic subsidence can better constrain the dynamic topography history and its underlying mechanisms.

In this study, we used forward landscape evolution simulations to investigate how surface processes respond to different dynamic topography models and orogenic flexures in continental North America. Particularly, we focused on the formation of key features in the Western Interior Seaway sedimentary records (Fig. 1; adapted from Robinson Roberts and Kirschbaum, 1995). These features (Fig. 1) include (1) spatially widespread sedimentary isopachs, and (2) temporally expanding and migratory depocenters. We first designed an orogeny model to investigate the surface responses to the orogenic effect itself. Then, we evaluated three dynamic topography models (Liu et al., 2008; Rubey et al., 2017; Müller et al., 2018) that are quantitative predictions from recent geodynamic models. These models have different spatiotemporal patterns of dynamic subsidence during the Western Interior Seaway formation and underlying physical mechanisms. By comparing the model results with the observed sedimentation patterns during the formation of the Western Interior Seaway, we aimed to provide constraints on (1) the extent of flexural subsidence in explaining the Western Interior Seaway, and (2) the dynamic topography history and the underlying mechanisms in the mantle. Based on the preferred model, we further investigated the surface manifestations of the dynamic topography, including its contribution to the sedimentation of the Western Interior Seaway with respect to orogenic flexure, and the initiation of regional Laramide uplift.

METHODOLOGY

Landscape Evolution Model

We used Badlands (Salles, 2016; Salles and Hardiman, 2016; Salles et al., 2018), an open-source landscape evolution model accounting for sediment erosion, transport, and deposition based on an unstructured mesh and a parallel framework. In Badlands, the governing equations describing key surface processes, i.e., erosion, sedimentation, diffusion, and flexure, are explicitly solved. Aside from these func-

tionalities, Badlands can also simulate features such as flexural response with spatially variable elastic thickness of the plate, orographic precipitation, and three-dimensional (3-D) heterogeneous erodibility, which were not utilized here. This code can effectively handle problems over various spatial and temporal scales. The capability of Badlands in simulating continental-scale landscape evolution over tens of millions of years makes it an ideal tool with which to test the interactions between surface processes and tectonic forcing due to different geodynamic histories of the mantle and the lithosphere.

In our study, we primarily focused on the interaction between tectonic subsidence (due to tectonic forcing) and sediment transport (due to erosion and sedimentation), with the governing equation of this process being

$$\frac{dZ}{dt} = -\nabla \cdot q + \dot{u},\tag{1}$$

where Z is elevation (m), \dot{u} is subsidence rate (m/yr), and q is sediment flux (m²/yr). For downslope sediment transport, the detachment-limited case was assumed, and the transport rate

involved channel flow and hillslope diffusion, following

$$-\nabla \cdot q = -\epsilon A^m (\nabla Z)^n - \kappa \nabla^2 Z, \qquad (2)$$

where ϵ is erodibility (1/yr), A is drainage area (m²), κ is diffusivity (m²/yr), and m and n are positive constants. The first term on the righthand side represents sediment transport by fluvial processes, while the second term is diffusion by soil creep (Chen et al., 2014, and references therein). Both ε and κ depend on lithology, precipitation, and channel hydraulics (Whipple and Tucker, 1999; Lague et al., 2005) and are scale dependent (Dietrich et al., 1995). The coefficients m and n indicate how the shear stress exerted on channel beds scales with discharge and slope under arbitrary conditions. Since the term for sediment transport is an empirical equation, there are no universal values for m and n, except that they are generally positive, with the m/n ratio considered to be ~0.5 (Tucker and Hancock, 2010). In Equation 2, A is a proxy for discharge that numerically integrates the total area and precipitation from upstream-connected nodes. Upstream-connected nodes are defined using a single-flow direction algorithm (SFD), where water discharge is routed following the steepest decent direction (O'Callaghan and Mark, 1984). The values of these parameters in our model were consistent with studies at similar spatiotemporal scales (Salles et al., 2017; Ding et al., 2019; Chang and Liu, 2019).

In Badlands, while the bedrock erosion rate is governed by Equation 2, the sediment deposition is implemented separately. Deposition occurs when (1) there is a topographic depression (pit), (2) the elevation is below the base level (sea level), or (3) the local topographic gradient is below a critical aggradational slope. These three conditions also limit the amount of deposition. If the amount of sediments is not enough to fill an inland basin at a particular elevation above sea level, the remainder of the accommodation space is filled with water up to a user-defined thickness to mimic lakes. Deposited sediment can be treated differently from bedrock in Badlands. For example, underwater sediments can be further transported downslope by postdepositional diffusion. Badlands simulates the source-to-sink process, obeying mass conservation. That is, the amount of mass due to erosion equals that of deposition plus outflow.

For simplicity, we neglected sediment compaction associated with deposition so the porosities of the bedrock and the deposited sediments were made equal. For the simulations, considering sedimentary porosity would increase the overall predicted sediment thickness and the consumption rate of accommodation space.

However, we assumed that the sedimentary porosity has little effect on the large-scale sediment distribution, which is controlled mainly by tectonic forcing. Hence, it is justifiable to ignore sediment compaction for the focus of this study.

Another important component in landscape evolution is flexure, i.e., the elastic bending of the tectonic plate due to loading or unloading. The governing equation for flexural deformation is:

$$D\nabla^2\nabla^2\omega + \Delta\rho g\omega = q_l \tag{3}$$

where ω is the vertical adjustment of the elastic plate (m), $\Delta \rho$ is the density contrast (kg/m³) between the mantle and the loading material (water, sediment, or a combination of the two), g is gravitational acceleration (m/s²), and q_l is the amount of stress (Pa) due to loading or unloading. D is the flexural rigidity (Nm) of an elastic plate defined as

$$D = \frac{ET_e^3}{12(1 - v^2)} \tag{4}$$

where E is Young's modulus (Pa), v is Poisson's ratio (dimensionless), and T_e is the effective elastic thickness (m) of the plate. In Badlands, flexural isostasy is solved using gFlex (Wickert, 2016), a software package designed to compute flexural deflection for Earth's surface.

Initial Conditions

Our area of interest in the landscape evolution simulations covered the continental United States, southern Canada, and northern Mexico, discretized with 5 km grid resolution (Fig. 2). To approximate the mid-Cretaceous topography of North America at the beginning of the Western Interior Seaway (ca. 100 Ma) as the initial topography, we took the following steps.

First, we calculated the total flexural-isostatic adjustment due to the Pleistocene Laurentide ice sheet based on ICE-5G (Peltier, 2004) and

removed that from the inferred bedrock topography at the Last Glacial Maximum (ca. 21 ka) to estimate a preglaciated topography. The removal of the glacial effect would yield a more realistic paleotopography for eastern North America.

Then, we flattened middle North America, where the Cretaceous sediments of the Western Interior Seaway basin now exist, down to ~50 m in elevation. In doing so, this region was low enough for a sizeable seaway to form with a subsidence magnitude as little as a few hundred meters, which is typical for published dynamic topography models. We made this region flat because the paleotopography underneath the Cretaceous sediments is rather unconstrained, and a flat topography represents a simple initial condition, suitable for our focus on the first-order, regional sedimentation patterns.

Finally, we added a mountain belt peaking at ~2 km to mimic the Sevier orogen that had started to develop prior to the mid-Cretaceous following geological proxies (DeCelles, 2004; Yonkee and Weil, 2015). The eastern front of the mountain belt was delineated by the observed western boundary of the Western Interior Seaway sedimentary basin (Fig. 1). We generated natural-looking river valleys in this mountain belt by first running the simulation without any tectonic forcing. In the simulation, this mountain belt had an adjustable height and extended across the entire west coast of North America. Note that the region west of this mountain belt was out of the scope of this study and had essentially no impact on the landscape evolution of the Western Interior Seaway, because the mountain belt acted as a topographic barrier.

Boundary Conditions

In the simulations, we implemented two tectonic components: orogeny and dynamic topography. The Sevier orogeny was coeval with the early phase of Western Interior Seaway and is traditionally considered as the primary source of sediments for the Western Interior Seaway.

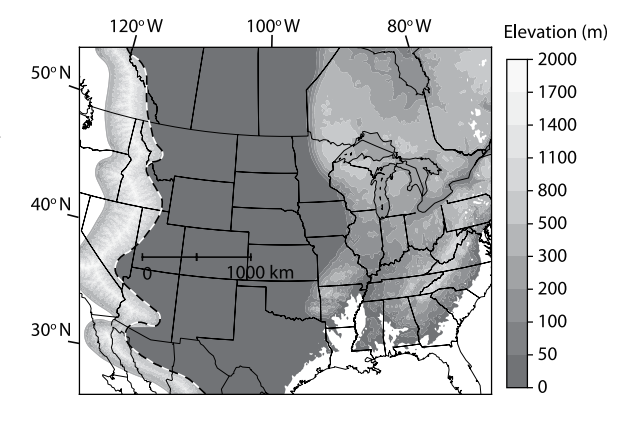
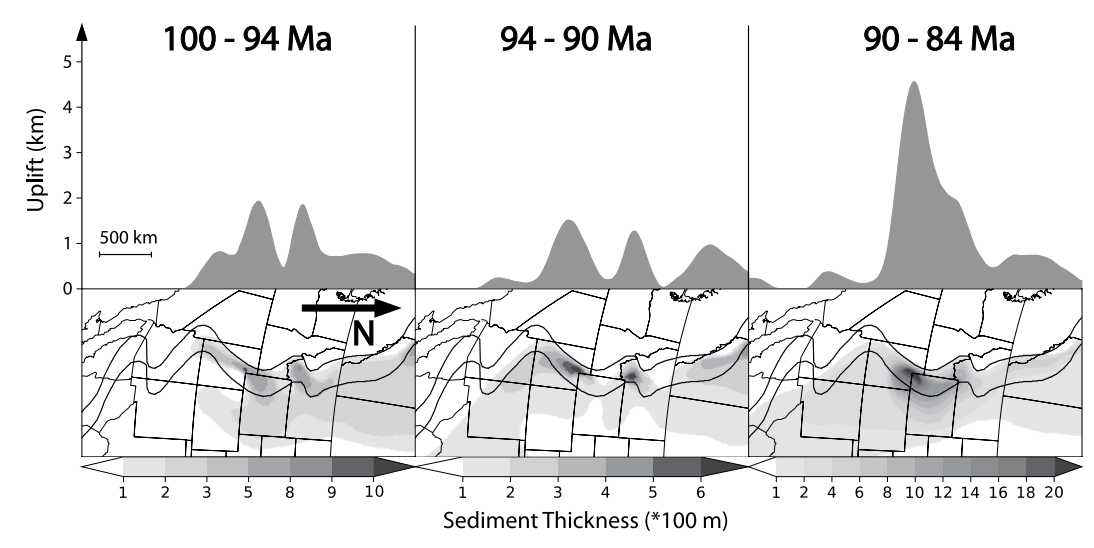


Figure 2. Input initial topography with an orogen on the west, flattened continental interior, and modeled preglaciated topography on the east. The thick black-white dashed line is the western edge of Western Interior Seaway sedimentation. Orogenic uplifts in the simulation will occur in the western orogen on this map. The color intervals are adaptive to better visualize the low topography.



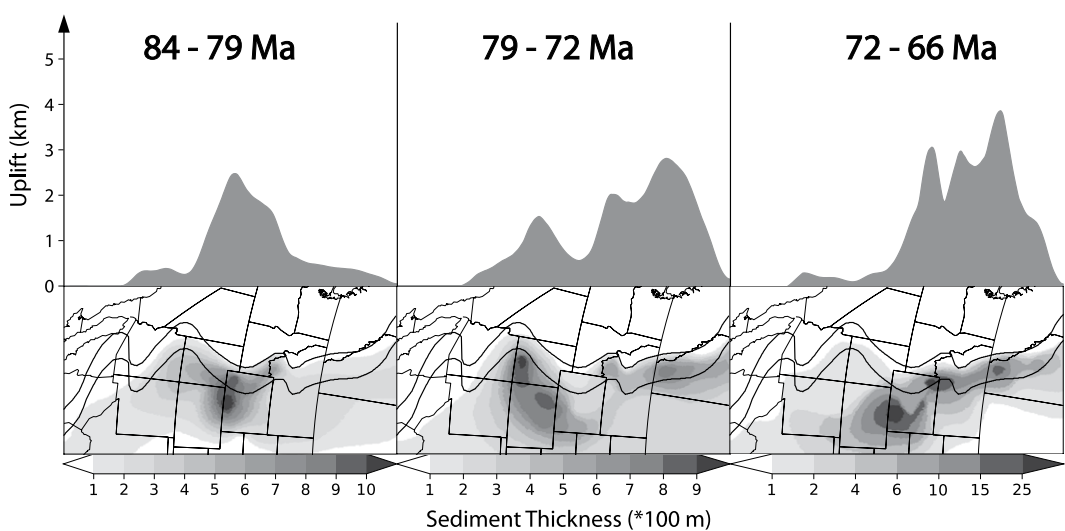


Figure 3. North-south profiles of orogenic uplift and the sediment distributions for the six episodes as in Figure 1. The region between the two black line in each episode indicates where the total sediment thickness was used to calculate the orogenic uplift profile.

Both the orogeny-induced flexural subsidence and the uplift-induced erosion have impacts on the Western Interior Seaway sedimentation history. During its later stage, the Sevier orogeny transitioned into the Laramide orogeny farther east. Here, we neglected the local Laramidestyled uplifts in the simulations because we focused on investigating the large-scale effects of dynamic topography on surface processes during the formation of the Western Interior Seaway. In fact, a recent study suggested that most significant uplift of Laramide ranges occurred after the Western Interior Seaway (Fan and Carrapa, 2014). In addition, inclusion of Laramide uplift in the topographic history would complicate the Western Interior Seaway sedimentation pattern, making it difficult to analyze the effects of dynamic topography.

Orogenic Uplift and Flexural Subsidence

The patterns of the input Sevier orogenic uplift and flexural subsidence in the simulations

were based on the observed sedimentation in the Western Interior Seaway over several episodes of the Late Cretaceous (Fig. 3), assuming local sedimentation patterns next to the Sevier belt should reflect orogenic loading. For the temporal variation of the input orogeny, there were six depositional episodes provided in the observational data, so we changed the uplift pattern from episode to episode and kept it constant within each uplift episode. We varied the spatial pattern of the orogenic uplift only in the north-south direction, along the strike of the Sevier orogeny. The total orogenic uplift at each latitude was determined by a linear transformation of the amount of sediment in the area that extended 250 km (an upper bound) eastward from the eastern front of the uplift, as illustrated in Figure 3 (between the two curves in each isopach map). This represents a maximum estimate of the orogenic loading for the observed sediment in the Western Interior Seaway foreland basin.

Below is the mathematical notation for the calculation of the uplift patterns based on the sedimentary isopach data:

$$u_{orog}(t,y) = F(t) *V(y,t),$$
 (5)

$$F(t) = \frac{1}{\max\{V(y,t) : y = 1, ..., N_y \mid t\}} \\ * \frac{\sum_{y} V(y,t)}{\sum_{t} \sum_{y} V(y,t)} * U$$
 (6)

where u_{orog} is the total rock uplift in the mountain belt as a function of location and time, V(y,t) is the sediment volume in the foreland area nearby, t is the uplift time, F is the function for the linear transformation in an episode, y is the node index along latitude, N_y is the number of nodes in the north-south direction, and U is an adjustable scaling factor to vary the overall amount of uplift. We also considered the sediment within ~80 km in the north-south direction in the actual calculation of the total sediment (V)

at each latitude (y). Such linear transformation can be validated by comparing the resulting sedimentation pattern with that observed, which is presented in the "Sedimentation Pattern in S0" section below. This scheme was used to simplify the process of varying the amount of orogeny to a simple number (U), herein named the "uplift scale," when testing how orogenic intensity affects sedimentation pattern. Specifically, the amount of orogenic uplift, at any location and time, scales proportionally to the amplitude of uplift (Equations 5 and 6). In Figure 3, the value of uplift scale is 18 km.

We assumed that the sediment outlined by the black curves in Figure 3 represents the foreland basin sediment. Hence, the volume of foreland sediment serves as a good proxy for the intensity of the concurrent orogenic uplift. As the amount of sediment in the southern Sevier foreland greatly diminishes after ca. 84-79 Ma (Fig. 3), the input orogeny uplift along the southern Sevier belt also diminishes in the simulations. This approximation of the Sevier uplift history is also consistent with its transition to the Laramide orogeny ca. 84-80 Ma, as observed (DeCelles, 2004; Yonkee and Weil, 2015). In the northern (Canadian) part, uplift in the Sevier belt continued until the Eocene (Tufano and Pietras, 2017), so the uplift after the 84-79 Ma episode in the model input reflects the continued uplift of this region (Fig. 3). We did not consider the gradual, ~200 km eastward progression of the Sevier orogeny (Yonkee and Weil, 2015) in the simulations because our orogenic model is based on a low-resolution sedimentary isopach (Fig. 1) that does not provide enough resolving power for the lateral migration of the load. In this case, the simulations are unable to capture the eastward progression of the foreland depocenter since input flexural subsidence is fixed. Nevertheless, the distance of such load progression is too small to affect the much more widespread landward Western Interior Seaway sedimentation or to explain the ~800 km depocenter migration (Fig. 1).

For the calculation of flexural subsidence, we used the pattern of total uplift in each episode with rock density equal to 2750 kg/m³ for the loading, and 20 km, 60 km, and 120 km for the lithospheric elastic thickness ($T_{\rm e}$). The chosen $T_{\rm e}$ values correspond to the flexural rigidities of $10^{22.7}$, $10^{24.1}$, and $10^{25.0}$ N·m, respectively. We used gFlex (Wickert, 2016) to calculate the flexural isostasy in the foreland due to the orogenic loading. Since the uplift scale (U) controls the amount of uplift, which is also treated as the load in the setup, its value also determines the magnitude of flexural subsidence in the foreland. We applied this combination of orogenic uplift in the mountain belt

and flexural subsidence in the surrounding foreland for each episode in every simulation. Note that this flexural subsidence due to the orogenic loading is independent from the flexural-isostatic response due to sediment loading or unloading. In this study, the former is an input boundary condition, while the latter is always implemented in the simulations and is fully coupled with the evolution of sediment transport. Note that the flexural subsidence pattern will be reported in the Results section (see sections on "Landscape Evolution in S0" and "Sedimentation Pattern in S0").

Dynamic Topography Models

For dynamic topography, we considered three different models from recent studies (Liu et al., 2008; Rubey et al., 2017; Müller et al., 2018), all of which predict subsidence in the western United States during the Late Cretaceous due to the subduction of the Farallon slab. All three models are from geodynamic simulations that assimilate realistic plate reconstructions. However, these models differ greatly in the predicted patterns of dynamic subsidence near the Western Interior Seaway, primarily because of their different approaches in estimating the past configuration of the Farallon slab, related to the methods for assimilating mantle density features and the adopted mantle viscosity structures.

Among these dynamic subsidence (DS) models (Fig. 4), DS1, based on M7 in Müller et al. (2018), is constrained by the observed global paleoshorelines and continental flooding patterns; DS2, the best-fit model in Liu et al. (2008), is constrained by the observed sediment thickness and paleoshorelines of the Western Interior Seaway; and DS3, from Rubey et al. (2017), is constrained by backstripping well data globally. In particular, the DS1 and DS2 models consider the flat subduction of the Farallon plate. Figure 4 illustrates the dynamic topography for these models at 100, 90, 79, and 66 Ma, corresponding to the temporal boundaries of every two uplift episodes. Comparatively, DS2 and DS3 have larger magnitudes (~1000 m) of subsidence, and DS2 has the strongest signal of eastward motion but shortest wavelength of the subsidence pattern. The large variations in the spatiotemporal patterns of subsidence among these models, when evaluated against the observed sedimentary records, can help us to better understand the dynamic origin of the Western Interior Seaway subsidence history.

Note that Figure 4 shows the absolute dynamic topography at each time step instead of the uplift rate. To make dynamic topography a tectonic component in the landscape evolution simulations, we obtained the uplift rate by taking the difference between two dynamic topography

snapshots divided by the corresponding time interval. Since the dynamic topography at the present is nonzero for these models, we also corrected the initial topography by accounting for the difference in dynamic topography between 100 Ma and the present day.

Besides the apparent differences in the patterns of these dynamic subsidence models, the choice of these models was also based on their geodynamic implications. DS1 is the latest model with a parameterized flat slab beneath the western United States. It takes advantage of up-to-date global plate reconstructions and mantle seismic tomography, and it considers thermochemical mantle layering and hot plumes (Müller et al., 2018). DS2 is based on an inverse convection simulation starting from present-day tomography that reproduces flat-slab subduction beneath the Cretaceous Western Interior Seaway. We emphasize that the DS2 dynamic topography was constrained specifically using well data within the Western Interior Seaway (Liu et al., 2008), and it has been shown to match the migratory subsidence as well (Liu et al., 2011). Finally, the DS3 model does not consist of flat-slab subduction below the Western Interior Seaway (Rubey et al., 2017). Dynamic topography in DS3 represents broad subsidence above a shallow-dipping slab, similar to an early conceptual model (Mitrovica et al., 1989).

With these three different dynamic subsidence models, our goal was to (1) quantify the Western Interior Seaway subsidence history by further considering the landscape evolution, and (2) identify the mantle dynamic processes underlying Western Interior Seaway sedimentation.

Simulations and Parameters

To achieve the research goals, we tested four tectonic scenarios. The first scenario (S0) included the orogenic uplift and thus flexural loading only, while the rest (S1-S3) used a combination of orogenic uplift and a specific dynamic subsidence history (DS1-DS3). Therefore, scenario S0 helped to investigate the orogenic effects on the Western Interior Seaway sedimentation pattern without any dynamic subsidence. We ran all simulations for 35 m.y., covering the entire Late Cretaceous (100-65 Ma). For the model parameters of landscape evolution, we tested three important factors: bedrock erodibility (ε), elastic thickness (T_{ε}), and uplift scale (U). The values of these parameters were empirically constrained, and we varied these values to test their effects. For each simulation, the values for these parameters were held constant. We used bedrock erodibility to representvthe general

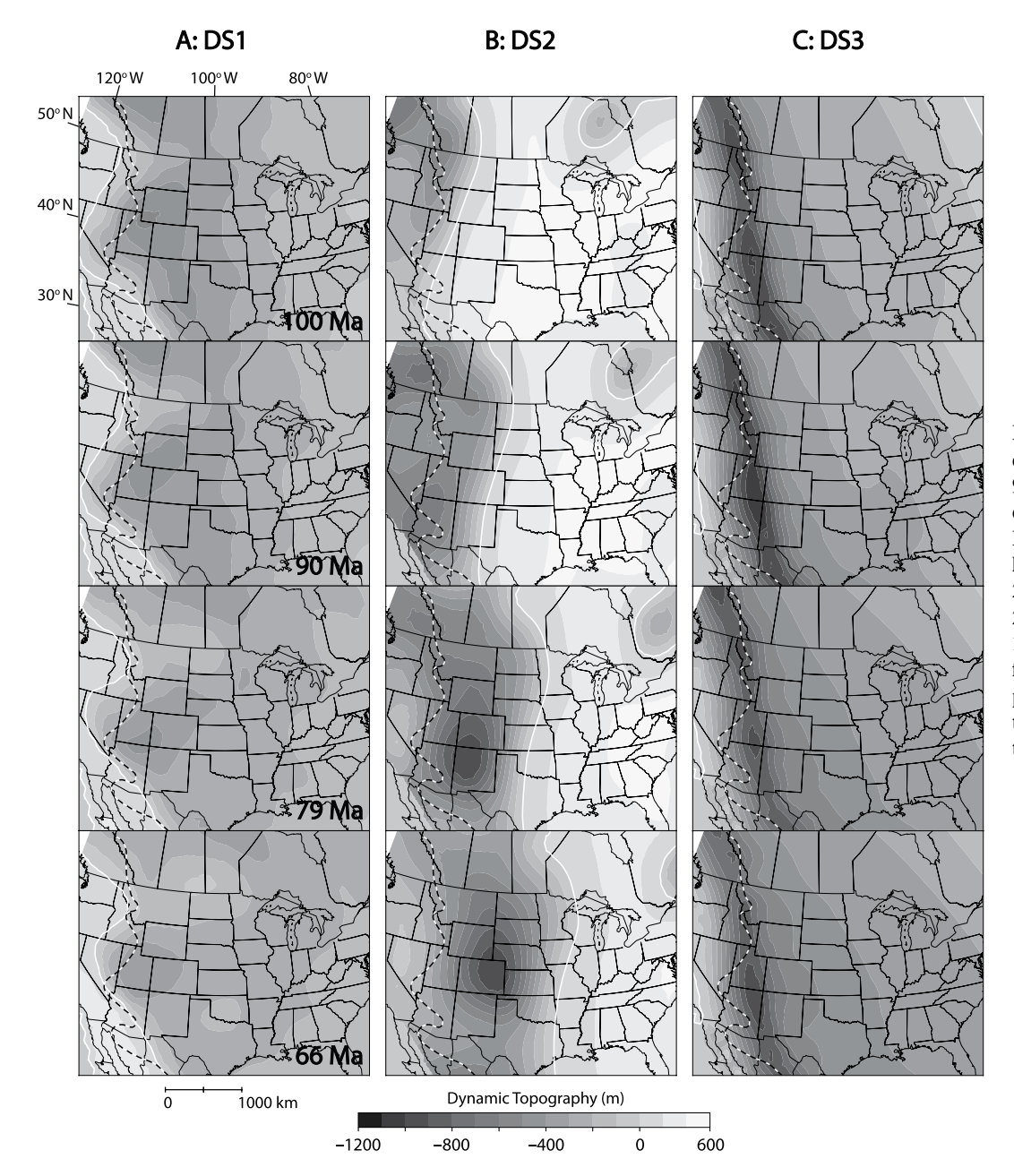


Figure 4. Snapshots of total dynamic topography at 100, 90, 79, and 66 Ma for the three dynamic subsidence models. From left to right: DS1 (Müller et al., 2018), DS2 (Liu et al., 2008), and DS3 (Rubey et al., 2017). The color interval is 100 m for negative and 200 m for positive dynamic topography. The white line indicates the contour for zero dynamic topography.

vigor of surface processes, including erosion and climatic forcing. For all simulations, the rainfall was fixed at 1 m/yr, and diffusivity (κ) was fixed at 1 m²/yr to avoid numerical instability. Table 1 offers a detailed description of the model parameters and their values.

RESULTS

Landscape Evolution in S0

Figure 5 demonstrates a result of the landscape evolution in S0 with topography (background colors), major sediment-rich rivers (black lines), and the cumulative orogenic flexural subsidence (red contours) at the ends of the six uplift episodes (94, 90, 84, 79, 72, and 66 Ma). With 21 km uplift scale (U), 2×10^{-7} yr⁻¹ bedrock erodibility (ϵ), and 120 km elastic

thickness ($T_{\rm e}$), this simulation represents a case of large-amplitude and wide-wavelength flexural subsidence and can depict the maximum

TABLE 1. MODEL PARAMETERS FOR THE LANDSCAPE EVOLUTION SIMULATION

Parameter	Value	Units
Grid size	5	km
Sea level (constant)	0	m
Underwater flow depth	150	m
Precipitation rate	1	m/yr
Max. lake water depth	200	ḿ
Erodibility	1, 1.5, 2,, 4.5, 5 (×10 ⁻⁷)	yr ^{−1}
Critical aggradational slope	10-4	m/m
Subaerial topographic diffusivity	1	m²/vr
Marine bedrock diffusivity	2	m²/yr
Marine sediment diffusivity*	10	m²/yr
Elastic thickness	20, 60, 120	km
Unlift scale	12 15 18 21	km

*Marine bathymetric diffusivity refers to diffusion of bedrock, while underwater sediment diffusivity refers to alluvial diffusion, both of which are treated separately in Badlands (see "Landscape Evolution Model" section).

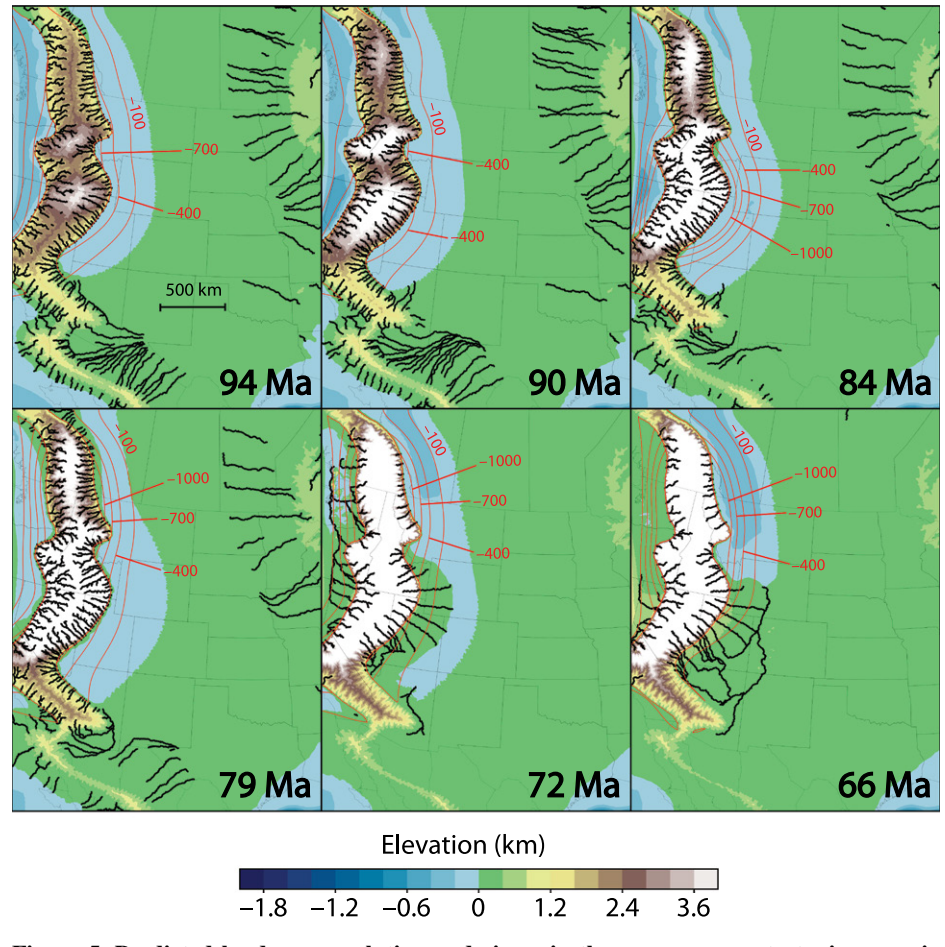


Figure 5. Predicted landscape evolution and rivers in the pure-orogeny tectonic scenario (S0) at the ends of the six uplift episodes (94, 90, 84, 79, 72, and 66 Ma) with the total flexural subsidence in each episode (red contours). Here, bedrock erodibility = 2×10^{-7} yr⁻¹, elastic thickness = 120 km, and uplift scale = 21 km. Note that the color interval for the submerged area (below sea level) is half of that for the subaerial area.

extent of orogenic effects. Figure S1¹ offers an S0 simulation with less extreme flexural rigidity ($10^{24.1}$ N·m; $T_{\rm e}=60$ km) and smaller orogenic uplift (U=18 km) than those presented in Figure 5. In this simulation, the uplifted orogen itself enhances erosion and provides the source of sediments, while the resulting flexural subsidence creates the depression in the foreland as the sink for the sediments. Since the orogenic uplift and the flexural subsidence are confined to the western region, the topography of the continental interior and the drainage pattern east of the flexural forebulge stay rather stable.

The S0 landscape simulation demonstrates that a seaway of more than 1000 km in width, such as

the Western Interior Seaway (Fig. 1), could not form from flexural subsidence, and that the rivers from the west carry sediments only to the foreland with very limited eastward progression. Mostly, the predicted inland sea is narrower than 500 km in the east-west direction, because the width of the inland sea is limited by the location of the flexural forebulge. Although the wavelength of flexural subsidence can increase with increasing flexural rigidity, it can never reach beyond 500 km given the typical values of flexural rigidity. The flexural subsidence achieved this way is also unable to generate the eastward-migrating topographic depression as implied from Western Interior Seaway sedimentation (Fig. 1). Note that Figure 5 represents a rather extreme case for the flexural effect. Hence, flexural subsidence due to orogenic loading cannot explain the formation of the Western Interior Seaway, consistent with recent studies claiming the dominant role of dynamic topography (Liu et al., 2008; Rubey et al., 2017; Müller et al., 2018).

Sedimentation Pattern in S0

Figure 6A demonstrates a representative result of the sedimentation history in S0 (blue colors) compared to the observed Western Interior Seaway isopach (red contours; adapted from Robinson Roberts and Kirschbaum, 1995) for the six uplift episodes (100-66 Ma). The model parameters are the same as those in Figure 5. In general, the sedimentation pattern closely follows that of the flexural subsidence and explains why the predicted inland sea remains mostly shallow, <200 m in depth (Fig. 5). The predicted sediment distribution and thickness can explain most of the observed values in the foreland for each uplift episode in the western United States. Although the foreland sediments in northern Alberta, Canada, are underpredicted during 94-84 Ma, they are less significant relative to the foreland sediments in the southern Western Interior Seaway. Therefore, these results suggest that the orogenic uplift inputs are largely valid, such that foreland basin sediment can be used as a proxy for orogenic uplift. Particularly, the predictions nicely capture the observed alongstrike locations of the sediment depocenter. Moreover, the S0 prediction agrees with the observation (Fig. 3) in that sediment accumulation is distributed within the Sevier foreland basin during 100-84 Ma for the southern Western Interior Seaway, where subsequent eastward progression of depocenter is significant. In the northern Western Interior Seaway, such agreement exists during 79-66 Ma. This implies that the orogenic effect largely controlled the location of most intensive sediment accumulation for the early stage of the Western Interior Seaway (100-84 Ma) in the south, but for the later stage (79-66 Ma) in the north.

However, the predicted basin widths² in general and the sediment quantity in the south are both too small compared to observed sedimentation (Fig. 6A). An additional simulation with ~60 m sea-level rise during 100-92 Ma (Haq et al., 1987) suggests that the impact of increasing sea level on Western Interior Seaway sedimentation is very minor (Fig. S2 [see footnote 1]). In this case, the flexural forebulge still limits the extent of sedimentation because its magnitude (>100 m) overwhelms that of sea-level change (<60 m). It is also evident that maximum sediment accumulation occurs always at the edge of the input orogenic uplift (Fig. 6A), rendering ~800 km migration of the depocenter impossible with only flexural subsidence.

¹Supplemental Material. Five additional figures to support some arguments in the main text and to aid readers' understandings. Please visit https://doi.org/10.1130/GSAB.S.12275144 to access the supplemental material, and contact editing@geosociety. org with any questions.

²The basin width is herein defined by the width of the 200 m sedimentary isopach along the cross section

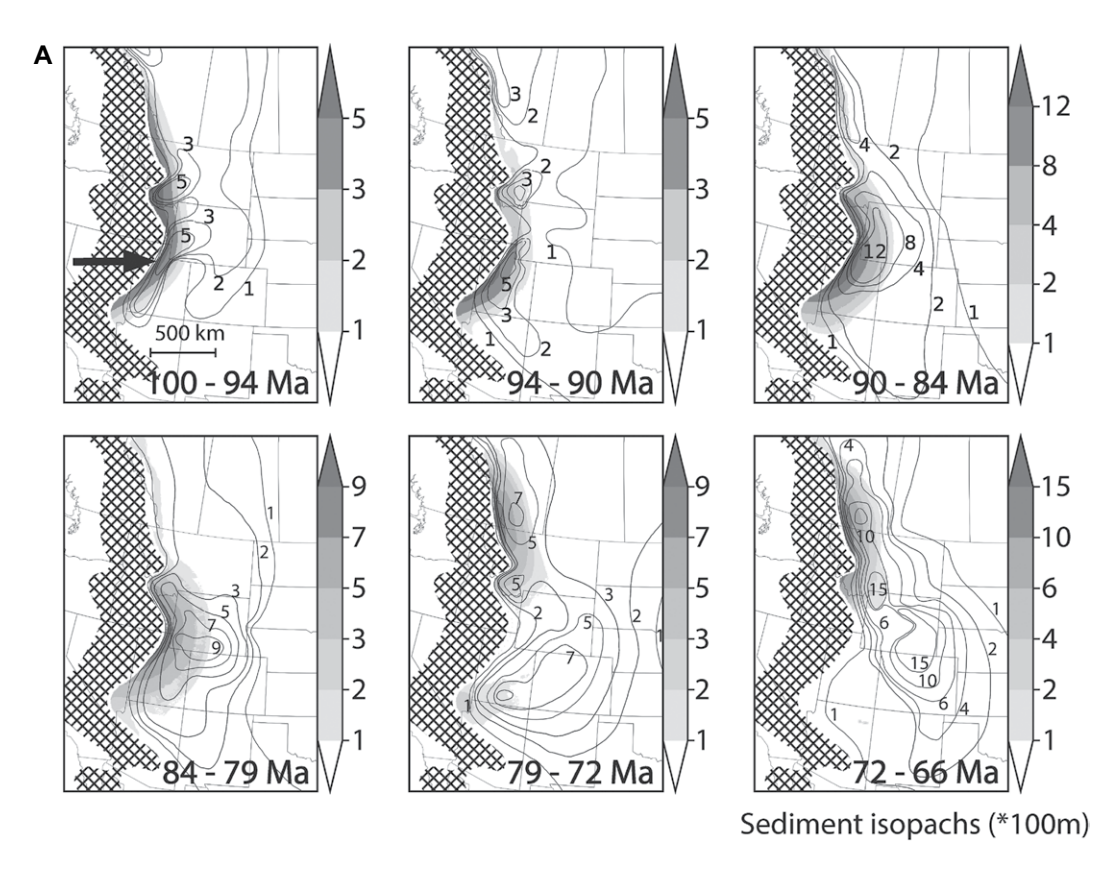
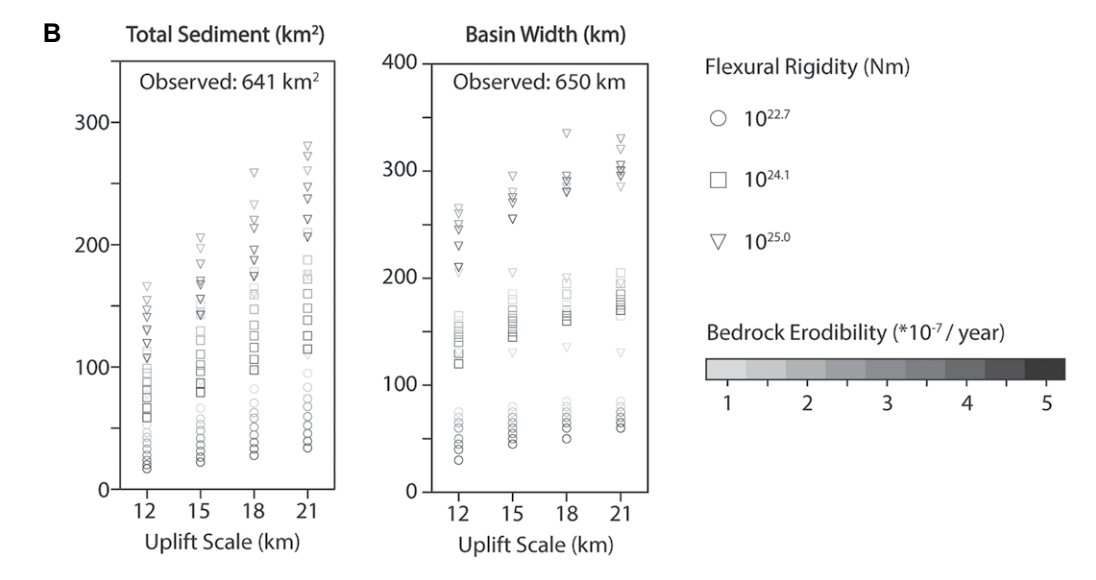


Figure 6. (A) Predicted sedimentation patterns (grayscale colors) in the six uplift episodes compared to those observed (black contours). Hatched region shows the orogenic zone. Black arrow indicates the latitude at which the uncertainty test was used to evaluate basin features and where the flexural inputs and responses are demonstrated. Here, bedrock erodibility = 2×10^{-7} yr⁻¹, elastic thickness = 120 km, and uplift scale = 21 km. (B) Uncertainty test on the total sediment and basin width (vertical axes), with bedrock erodibility (color-coded), flexural rigidity (shape-coded) and uplift scale (horizontal axes) in the third episode (90-84 Ma). The inline text indicates the observed value. The basin width is defined by the 200 m sedimentary isopach.



To better understanding the effects of other model parameters in the formation of the Western Interior Seaway based on pure orogenic loading (Figs. 5 and 6A), we performed an uncertainty test by further varying bedrock erodibility and flexural rigidity in this class of simulations. The uncertainty test was focused on the third episode (90–84 Ma), during which the input orogenic effect is most pronounced and the impact of initial topography should

already be relaxed. Figure 6B shows the results of the predicted area of sediment (left) and basin width (right) by varying bedrock erodibility, elastic thickness, and uplift scale, which are all influential parameters, in the cross section along the latitude specified by the green arrow in Figure 6A (upper-leftmost panel). The results demonstrate that both basin width and total sediment increase with increasing uplift scale and flexural rigidity, which control the magnitude and the

wavelength of flexural subsidence, respectively. Most importantly, this uncertainty test suggests that all combinations of these parameters fail to produce either the sediment quantity or basin width close to their observational values (shown in Fig. 6B). Hence, we conclude that flexural subsidence alone is unable to explain the spatial extent and thickness of Western Interior Seaway sedimentation, implying that additional subsidence further inland and later in time is required.

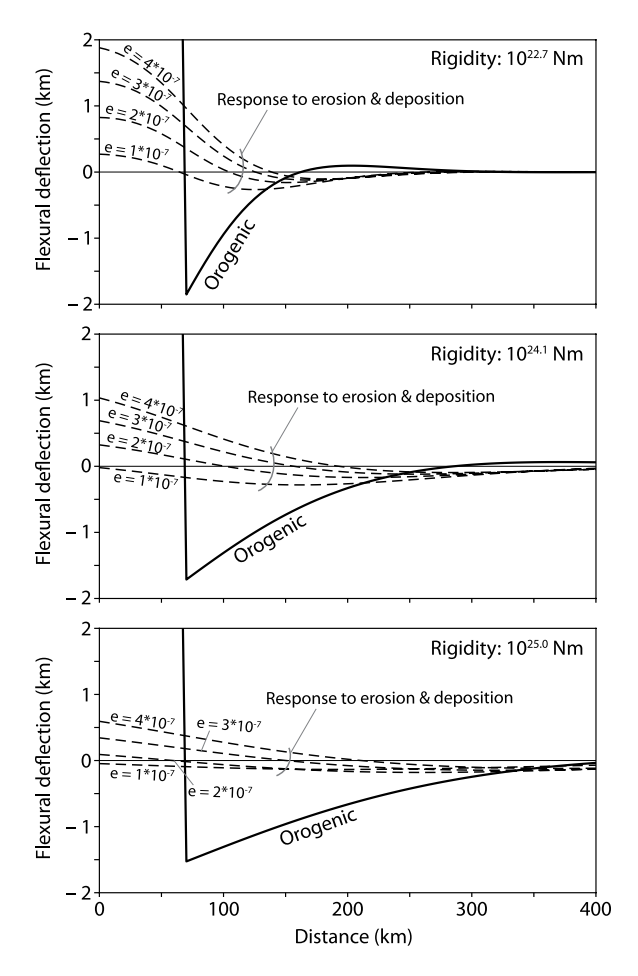


Figure 7. Orogenic flexure (solid black line) during 90–84 Ma with uplift scale = 18 km versus the cumulative flexural responses to erosional unloading over the same time period with different erodibilities (dashed lines), and small (top), medium (middle), and large (bottom) flexural rigidities.

Counterintuitively, the results in the uncertainty test (Fig. 6B) suggest that increasing bedrock erodibility generally leads to decreasing sediment quantity. The reason is that with a higher erodibility, the foreland experiences more flexural-isostatic uplift due to the enhanced erosion in the orogen, decreasing the orogenic loading, and so the accommodation space for foreland sediment is effectively reduced (Fig. 7; Figs. S1 and S3 [see footnote 1]). This trend is more prominent when flexural rigidity is smaller (Figs. 6B and 7) and exists on the condition that sediment accommodation space is filled. In the cases with 1025.0 N·m flexural rigidity, the trend between erodibility and sedimentation disappears because (1) the condition that accommodation space is filled quickly is invalid (Fig. S3 [see footnote 1]), and (2) the fractional reduction of accommodation space by erosional unloading decreases with larger flexural rigidity (Fig. 7). A key process here is the flexural response due to erosional unloading, the influence of which can propagate from the orogen into the foreland basin, and this behavior is indifferent to flexural rigidity (Fig. 7). Even though more sediment is produced via enhanced erosion, the reduced accommodation space with rapid sediment fill

(Supplemental Material [see footnote 1]) limits the total sediment deposition and eventually results in a smaller basin. As bedrock erodibility can represent the overall efficiency of surface processes, this result implies that erosion alone cannot expand the foreland sedimentation in a purely orogenic setting. To expand the foreland basin further inland, it requires a broader pattern of tectonic subsidence, such as that due to dynamic topography.

Landscape Evolutions in S1-S3

Figure 8 shows the representative results of the landscape evolution in S1–S3, with topography (background colors), major sedimentrich rivers (black lines), and the total dynamic subsidence (red contours) at 94, 84, 72, and 66 Ma. The model parameters U, ε , and $T_{\rm e}$ are 18 km, 3.5×10^{-7} yr⁻¹, and 60 km, respectively, for a more moderate orogenic load and flexural rigidity and an increased sediment supply compared to the case in Figures 5 and 6. A wide seaway (inundation of >1000 km wide) forms in each simulation over the Late Cretaceous due to dynamic subsidence. This suggests that all three dynamic topography models are useful to

explain the formation of the Western Interior Seaway, even though the detailed subsidence patterns differ. Since rivers are sensitive to topography, all major rivers in these simulations respond readily to the dynamic subsidence and transport sediment to the seaway (sink). Most of the sediment-rich rivers are from the orogen on the west, so the orogen is the major source of the sediment in the Western Interior Seaway. Therefore, all dynamic subsidence models used in this study can form a seaway that becomes the sediment sink.

In comparison, the dynamic topography in S2, which has relatively large magnitude and spatial migration, results in an eastwardmoving depression center and eastward shift of the entire seaway. The seaway in S1 is mostly shallow (<400 m deep) and shrinks over time, largely due to the dynamic rebound (Fig. 4A). In S3, the seaway forms similarly to that in S2, but with no migration of the depression center and little shift of the seaway. While the migration of the depression center depends entirely on the location of peak dynamic subsidence, the shift of the seaway depends additionally on sediment deposition, which increases local elevation and causes shoreline retreat. According to the predicted topographic depressions, only S2 can reproduce a depocenter ~800 km east of the Sevier orogen as observed (Fig. 1) among the three scenarios.

Furthermore, the shift of the seaway with time could greatly affect the continental drainage pattern. When the shift is significant enough, the drainage pattern would become unstable and adjust to the evolving landscape. Take S2 for example. The elevated eastern continent and the submerged middle continent east of the Sevier orogen create many significant sediment-rich rivers flowing westward during the early stage (before 84 Ma) of the predicted Western Interior Seaway, rendering the eastern continent a nonnegligible source of the sediment. During the later stage (after 84 Ma), the migration of dynamic subsidence submerges the eastern continent and raises the middle continent. This process decreases the drainage areas of the westward-flowing rivers from the east and increases those of the eastward-flowing rivers from the orogen. Therefore, the drainage pattern in S2 is the most unstable among the three scenarios over the Late Cretaceous, due to the migration of the dynamic subsidence.

Compared to S2, the seaways in S1 and S3 are mostly wider over the Late Cretaceous, a feature that seems more consistent with the inferred maximum extent of the Western Interior Seaway (Smith et al., 1994; Liu, 2015). As a result of the long wavelengths of the subsidence, such wide seaways create more area

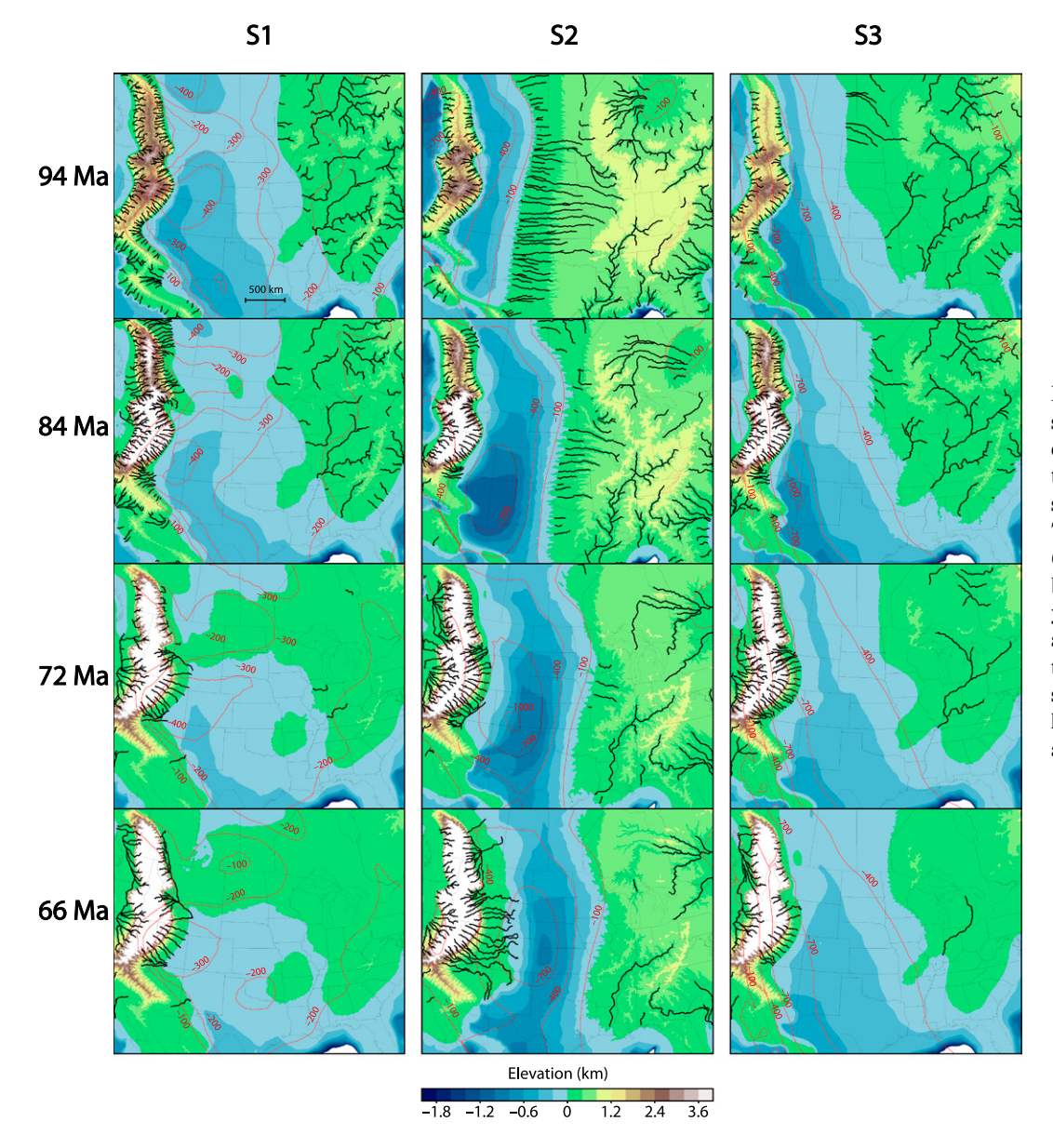


Figure 8. Snapshots of landscape evolution and river drainage pattern, with the contemporary total dynamic subsidence (red contours) at 94, 84, 72, and 66 Ma in S1 (left), S2 (middle), and S3 (right). Here, bedrock erodibility = 3.5×10^{-7} yr⁻¹, elastic thickness = 60 km, and uplift scale = 18 km. Note that the color interval for the submerged area (below sea level) is half of that for the subaerial area.

for sedimentation, but at the same time, they hinder the formation of rivers from the eastern continent and diminish the sediment derived in that region. In particular, there are also differences in the size of the predicted seaways over time among the three scenarios. The seaway in S1 starts out large and shrinks noticeably after 84 Ma, while those in S2 and S3 grow over time and start to expand or shift eastward sometime between 84 and 72 Ma, more similar to observation (Smith et al., 1994; Liu, 2015). In summary, even though a large seaway appears in each scenario, the spatiotemporal evolution of the predicted seaway varies significantly from one scenario to another. Consequently, these differences in landscape evolution lead to contrasting sedimentation patterns, as discussed below.

Sedimentation Patterns in S1-S3

Figure 9 shows the representative results of the sedimentation patterns for S1-S3 (blue colors), compared with observation (red contours), during the entire Late Cretaceous (100-66 Ma). Model parameters $(U, \varepsilon, \text{ and } T_e)$ are the same as those in Figure 8, and the S0 prediction (only flexural deformation is allowed) with the same parameters is shown in Figure S4 (see footnote 1). A common sedimentation feature among these three scenarios is a larger area with nontrivial (>100 m) sediment deposition than that in S0 (Fig. 6A), formed mostly after the first uplift episode. This is because the broad topographic depression across the middle North America, caused by the long-wavelength (>1000 km) dynamic subsidence, is able to accommodate sediments further landward (Fig. 8). In addition, dynamic subsidence in each scenario provides accommodation space in the foreland in addition to the flexural subsidence. The additional accommodation space allows intense sedimentation during the early stage of Western Interior Seaway (100–84 Ma) without requiring extreme flexural subsidence such as that in the pure orogenic loading case (Figs. 5 and 6A). Such intense sedimentation in the foreland subsequently wanes as the additional accommodation space from dynamic subsidence is consumed, and no further space is created over time. Thus, dynamic subsidence directly facilitates sedimentation within and beyond the foreland.

Notably, both the area with nontrivial deposition and the intensity of sedimentation in S2 are the largest among the three scenarios at all

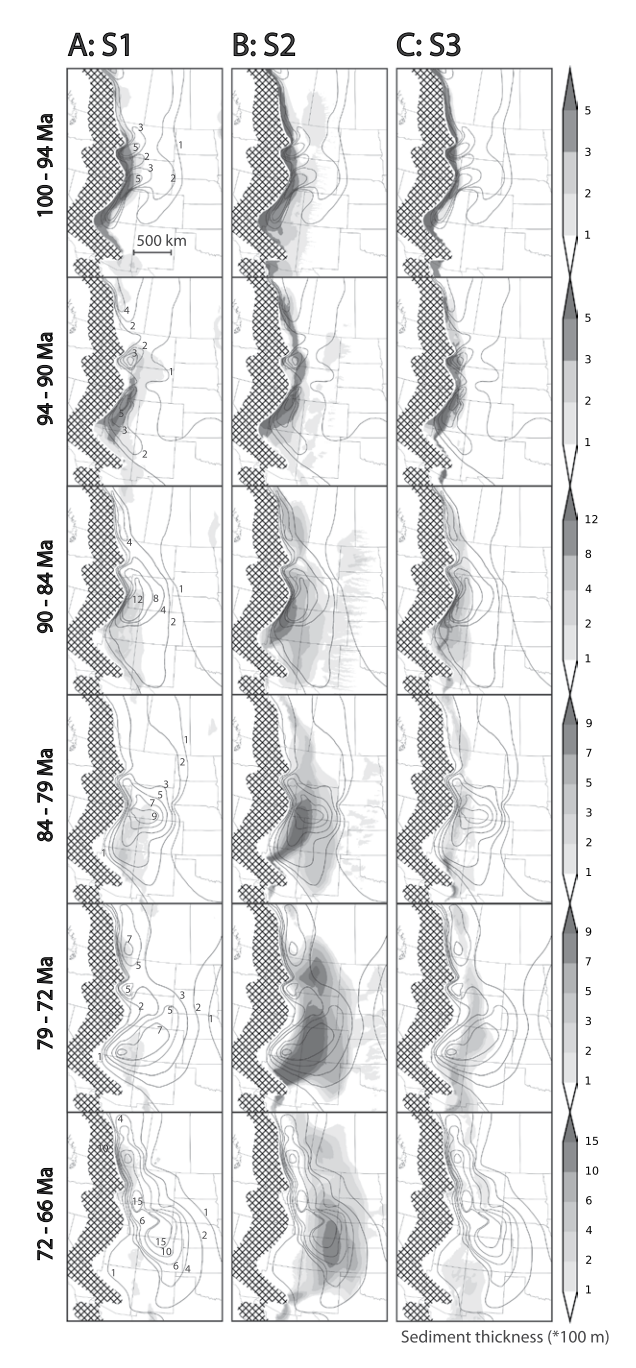


Figure 9. Predicted sedimentation patterns (grayscale colors) compared to the observation (black contours) for the six uplift episodes over the entire Late Cretaceous in S1 (left), S2 (middle), and S3 (right). Hatched region shows the orogenic zone. The contour values of observed isopachs are the same for all three scenarios (across the same row) and are only shown in the left panel. Here, bedrock erodibility = $3.5 \times 10^{-7} \text{ yr}^{-1}$, elastic thickness = 60 km, and uplift scale = 18 km.

times. Both phenomena can be explained by the magnitude and migration of dynamic subsidence in model DS2. Most importantly, sediment accumulation responds proportionally to the incremental subsidence, instead of the total subsidence. In turn, incremental subsidence depends on the change of dynamic topography, by either increasing the magnitude of subsidence or shifting the depression center. In the case of S1, model DS1 has a subsidence pattern that stays largely stationary over time, without migration or increase in magnitude. So, the lack of incremental subsidence severely prohibits

sedimentation; once the accommodation space from the initial subsidence is consumed, the sedimentation rate declines drastically after 94 Ma. Similarly, in the case of S3, the incremental subsidence in DS3 is insufficient to create the size of accommodation space comparable to that in S2. However, as the magnitude of subsidence in DS3 slightly grows larger over time, there is more incremental subsidence for sedimentation compared to DS1. In the end, only DS2, with its magnitude and migration, can constantly generate large amounts of accommodation space over time that allows sustained, intense sedimenta-

tion. Continued migration of DS2 also creates new accommodation space further eastward, resulting in the widespread area of inland sedimentation (Fig. 9B).

In a comparison between the prediction and the observations, the three scenarios perform similarly in the first two uplift episodes (Fig. 9). During this time, most of the predicted sedimentation takes place in the foreland, largely consistent with observations, despite the fact that the predicted area of nontrivial (>100 m) sedimentation is slightly smaller than observed in all scenarios. The predicted depocenters generally line up well with those observed, suggesting that flexural subsidence was the dominant control on the sediment distribution at the time. Meanwhile, the dynamic subsidence enhances foreland depression and expands the area of sedimentation. Smaller basin areas in predictions than those observed may reflect the uncertainty in dynamic subsidence models and that in the initial topography.

Starting from the third uplift episode (90 Ma), only S2 can produce most of the key features in the observed sedimentation patterns, namely, the wide area of sedimentation, the continuously intense sedimentation, and the eastward migration of the depocenter over time. Neither S1 nor S3 has these features in their respective predictions. As sedimentation closely follows the incremental subsidence, these sedimentation features reflect the increasing magnitude and eastward migration of DS2. Despite some local mismatches like those north of Wyoming, there is good consistency between S2 predictions and the observations over most of the western United States (Fig. 8B). Particularly, these include the agreements on the dispersion of sedimentation during 90-72 Ma and the apparent eastward displacement of the depocenter in the last uplift episode (72-66 Ma). Therefore, S2 can best explain the Western Interior Seaway sedimentation, and DS2 represents the most likely model for Western Interior Seaway dynamic subsidence. These results further suggest that the dominant control on sedimentation transitioned from flexural to dynamic subsidence after 90 Ma.

Finally, we present an uncertainty test for each scenario to examine the effects of bedrock erodibility, elastic thickness, and uplift scale on the output of total sediment, basin width, and the depocenter location, along the same east-west Western Interior Seaway cross section indicated in Figure 6A. The choice of this latitude for the uncertainty test came from the apparent east-ward progression of sedimentation over time as observed. Figure 10 reports the results for each scenario, with effects of variations of these three factors measured as numerical quantities, plotted for the corresponding scenario. The model

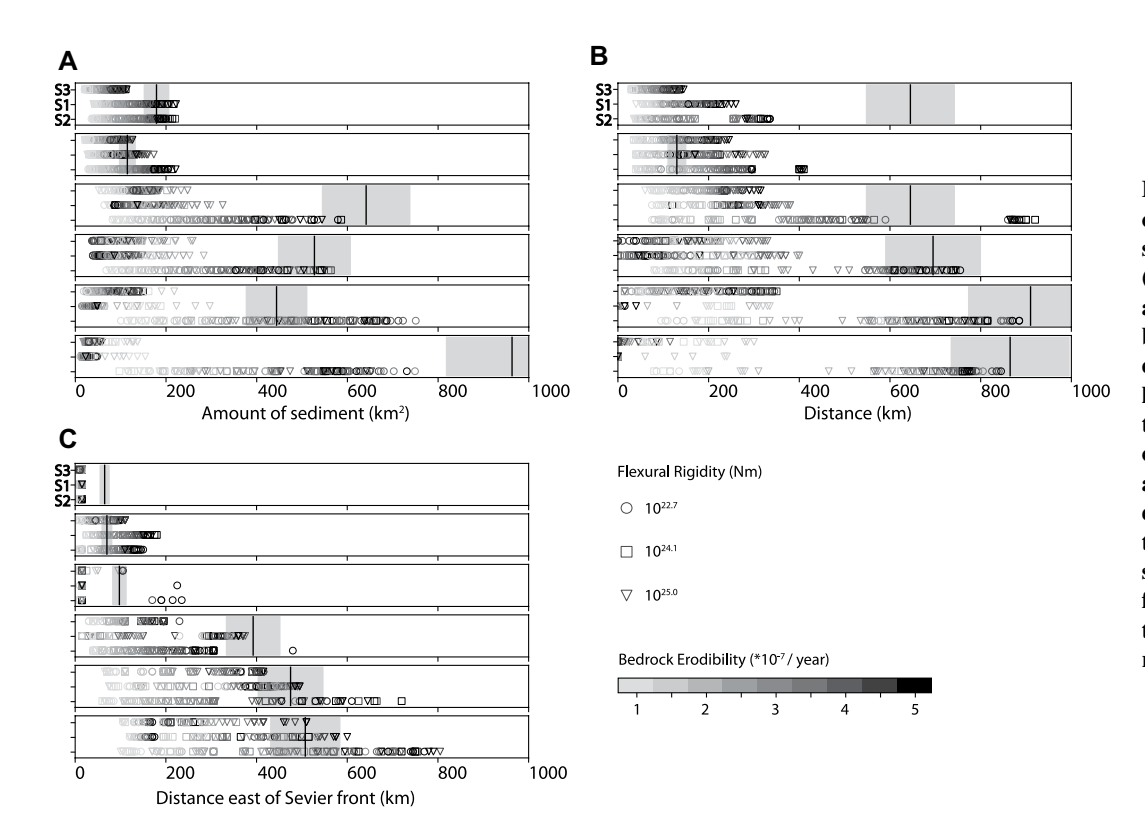


Figure 10. Uncertainty tests on the basin features: (A) total sediment, (B) basin width, and (C) depocenter location. S3, S1, and S2 are shown from top to bottom, respectively, in each episode (one subplot). Vertical lines and gray shades indicate the values derived from the observation with 15% tolerance range. The basin width is defined by the 200 m sedimentary isopach. The lower-right section shows the color code for bedrock erodibility and the symbol code for flexural rigidity.

values for each output basin feature are compared side by side with those observed allowing for a 15% tolerance range. The values of these factors follow those reported in Table 1. Note that only bedrock erodibility and flexural rigidity are specified here. The main goal of the uncertainty test was to check if each scenario can circumstantially reproduce the quantitative features in the observation by varying the values of these input factors $(U, \varepsilon, \text{ and } T_{\varepsilon})$.

The results of this uncertainty test (Fig. 10) show that the three scenarios perform similarly during the first two uplift episodes, confirming that the outcome sedimentation patterns are largely insensitive to the choice of dynamic subsidence model during this period. The fact that all three scenarios fail to predict the observed values of basin width and depocenter location in the first uplift episode (100-94 Ma) likely indicates inaccuracy of the initial topography, since the predictions can well fit the observed values in the second uplift episode (94-90 Ma). Sea-level change is unlikely to be the cause, given its small magnitude (<60 m), and it has an insignificant effect in this case (Fig. S2 [see footnote 1]). For the later four uplift episodes (90-66 Ma), however, the results suggest that the S2 predictions can most consistently fit the observed values (bottom rows in Fig. 10). This is especially clear for the total sediment and basin width, due to the appropriate magnitude and migration of DS2 as previously explained. Depocenter location, on

the other hand, is the least sensitive feature to the different scenarios of dynamic topography. Still, the overall trend suggests that after 90 Ma, dynamic subsidence dominated the sedimentation patterns, and S2 is the best scenario due to its likelihood to capture all observed basin features. Hence, the S2 scenario still performs the best after taking into account the variations of the three factors in landscape evolution.

DISCUSSION

Formation of the Western Interior Seaway

Based on the comparison between the observations and predictions in S0-S3, dynamic subsidence is a requirement for Western Interior Seaway formation. For the sheer size of Western Interior Seaway inundation and sedimentation, flexural subsidence due to orogenic loading alone is evidently insufficient (Figs. 5 and 6). Dynamic subsidence offers the long-wavelength (>1000 km) subsidence that is required to explain the Western Interior Seaway formation and sedimentation (Figs. 8 and 9). In this study, we used landscape evolution simulations to further affirm the studies proposing the need for dynamic topography in explanation of the Western Interior Seaway sedimentary records (DeCelles, 2004; Liu and Nummedal, 2004; Liu et al., 2005, 2014; Heine et al., 2008; Liu, 2015; Heller and Liu, 2016). We also show that this conclusion is indifferent to the parameters of landscape evolution, particularly the efficiency of surface processes.

Although orogenic effect alone is unable to explain the formation of the Western Interior Seaway, it has significant effect on the Western Interior Seaway sedimentation history. This study quantitatively attests that (1) in the Sevier foreland, flexural subsidence primarily controlled the distribution of intensive sedimentation, even with the presence of dynamic subsidence (Fig. 9), and (2) beyond the foreland, the orogeny provided the necessary sediment supply for sedimentation further landward (DeCelles, 2004; Yonkee and Weil, 2015). Particularly, the results highlight that when constraining the tectonic history with sedimentary records, both sediment supply and accommodation space are crucial considerations, where landscape evolution simulation has an advantage over traditional methods such as sedimentary backstripping (Chang and Liu, 2019). This study further demonstrates that foreland sedimentation history can serve as a valid proxy for orogenic evolution. The method herein may be less accurate than a detailed palinspastic reconstruction, but it provides a simulation-compatible and quantitatively constrained orogenic load model at the continental scale over tens of millions of years. Refining this orogenic load model, which is beyond the scope of this study, will be unlikely to change our main conclusion.

Furthermore, the dynamic subsidence during the Western Interior Seaway was likely large in magnitude (~1000 m) and moving eastward over time, consistent with previous studies (Liu et al., 2011; Chang and Liu, 2019). Among the three dynamic subsidence models, only DS2 has these features, and the resulting S2 simulation is the most likely scenario according to the visual comparison (Fig. 9). Although some landscape evolution parameters can manufacture the observed eastward migration of the depocenter in S1 and S3, only S2 can most consistently capture the intensity of sedimentation and basin width (Fig. 9). Hence, the most likely geodynamic mechanism for the Western Interior Seaway is the downward pull from the Farallon flat slab underneath the westward-moving North American plate, as proposed in the corresponding geodynamic models (Liu et al., 2008; Liu, 2015; Müller et al., 2016, 2018).

We find that the S2 simulation predicts by far the most sedimentation, and the reason lies in the continuing change of DS2, which in turn offers sustained incremental subsidence. We emphasize that it is the incremental subsidence, not the cumulative subsidence, that creates new accommodation space for sustained, inland sedimentation. We also note that the initial topography has little effect on the sustainability of inland sedimentation because the initial accommodation space will be quickly taken up by early sedimentation, after which other tectonic forcing will take dominance. Therefore, for dynamic topography models constrained by residual subsidence from sediment-backstripping, accurate age and depth information is important for quantifying the signal of incremental subsidence (Liu et al., 2011).

Since DS2 represents a plausible scenario for the past dynamic topography, we further investigated its detailed spatiotemporal impacts on the sedimentation history in the western-middle continent. The predicted sedimentation history can be characterized by three stages based on the relative importance of dynamic subsidence in forming the large-scale (>200 km) Western Interior Seaway sedimentation: (1) moderate in 100-90 Ma, (2) transitional in 90-84 Ma, and (3) dominant in 84-66 Ma. First, during 100-90 Ma, the sediment accumulates primarily in the Sevier foreland. The flexural subsidence mainly controls the along-strike depocenter location (Fig. 6A), while dynamic subsidence further enhances the depression, leading to wider sedimentation areas within the foreland basin (Fig. 9B). Then, during 90-84 Ma, the sediment accumulation starts dispersing eastward with a large portion still localized within the foreland. This is when dynamic subsidence begins to move the depocenter away from the

foreland. However, since the subsidence center is still close to the western orogen, the sedimentation pattern only shows eastward progression, not displacement. Finally, during 84–66 Ma, the sediment accumulation migrates eastward, out of the foreland, and the foreland sedimentation completely shuts down. The depocenter is ultimately displaced ~800 km east of the Sevier front. At this time, the dynamic subsidence dominates the control on sediment distribution.

Identification of the relative importance of dynamic subsidence in the observed Western Interior Seaway sedimentation history further reveals the underlying tectonic drivers for the Late Cretaceous subsidence in the middle continent. The timing at which the dynamic subsidence becomes important in the sedimentation distribution roughly coincides with emplacement of the proposed Shatsky conjugate plateau, because its initial buoyancy causes slab flattening at ca. 88 Ma (Liu et al., 2010). By reducing the slab dip angle, this oceanic plateau causes the dynamic subsidence, and in turn sedimentation, to migrate further inland to the continental interior. While the migration of dynamic subsidence comes from the relative motion between the subducting slab and the overriding plate, the temporally increasing subsidence magnitude reflects the accumulation of slab materials beneath the continent (Fig. 4). This interpretation is similar to that inferred from analyzing the residual subsidence of the Western Interior Seaway basin (Liu et al., 2011; Heller and Liu, 2016). However, in this study, we further quantified the surface manifestations of Farallon flat-slab subduction through tracking sediment transport and deposition using realistic landscape evolution simulations.

There are some notable mismatches present in the sedimentation patterns between the S2 predictions and the observations. Specifically, in the Western Interior Seaway region north of Wyoming, the basin width is consistently shorter than that observed after 90 Ma, and the predicted pattern poorly resembles the observation after 79 Ma (Fig. 9). Since the dynamic subsidence largely controls the sedimentation pattern after 90 Ma, these discrepancies mostly originate from the errors in DS2. Decreasing the efficiency of surface processes to keep the depocenter closer the orogen would not fix the mismatches, because the consequent amount of sedimentation would be too small. A possible explanation is the pure-thermal assumption of mantle density anomalies, which may miss the basalt-eclogite phase transition in the DS2 calculation, affecting both the local slab geometry and the induced dynamic subsidence (Liu et al., 2011). Alternatively, this could also be due to inaccurate mapping of mantle density structures using seismic

tomography (Liu et al., 2008). In addition to possible uncertainties in DS2, the orogenic effect (e.g., flexural rigidity) after 79 Ma in the north is likely underestimated in Figure 9 such that the simulation is unable to match the observed intense foreland sedimentation.

Despite some local discrepancies, DS2 still represents the most likely model in this study for the Late Cretaceous sedimentation history due to its appropriate subsidence magnitude and spatial migration. However, we note that DS2 merely represents one possible scenario from a collection of models that share similar subsidence patterns to that in DS2. Here, we emphasize that the goal of this study was to investigate the likely subsidence history causing the Western Interior Seaway and distinguish its underlying mechanism, instead of reproducing the exact Western Interior Seaway sedimentation history. Further matching of the Western Interior Seaway stratigraphy would require more sophisticated subduction models and landscape evolution simulations.

We further explored the effect of landscape evolution parameters on the Western Interior Seaway sedimentation. Figure 10 suggests that bedrock erodibility, the proxy for the overall intensity of surface processes, is an important parameter. In general, the values of all three features grow with increasing bedrock erodibility. Such a trend is most prominent during 100–90 Ma (upper two subplots in each panel), regardless of the dynamic topography model, because the accommodation space exceeds the sediment supply in the southern Western Interior Seaway. After 90 Ma (lower four subplots in each panel), this trend fails for total sediment quantity in S1 and S3 (top and middle rows in each subplot), due to the scarcity of incremental accommodation space in this region. In effect, a large sediment supply due to high bedrock erodibility can deplete the initial accommodation space before 90 Ma, and then without creation of additional accommodation space due to increased subsidence after 90 Ma, the regional sedimentation declines. In contrast, S2 (bottom row in each subplot) has continuous creation of accommodation space so the trend holds in every episode. These results re-emphasize the importance of the creation of accommodation space for continued inland sedimentation. However, this uncertainty test suggests that no universal, best-fit values exist for any landscape evolution parameters (Fig. 10; Fig. S5 [see footnote 1]), except that a large (> $2.5 \times 10^{-7} \text{ yr}^{-1}$) bedrock erodibility is generally preferred in S2. A detailed analysis of these input parameters is beyond the scope of this study.

Finally, by differentiating and evaluating several plausible dynamic topography models using

landscape simulations, this study highlights the importance of taking surface processes into account when constraining past dynamic topography. When the sedimentary record represents the primary constraint for the tectonic history, comprehensive analysis of source-to-sink sediment transport is especially important. Conventionally, geodynamic models often rely on limited geologic constraints, omitting the responses in surface processes, for calculating dynamic topography. This study suggests that landscape evolution simulations can further constrain the subsidence history by directly examining the predicted surface responses. Therefore, future dynamic topography models can make use of landscape evolution simulations as part of the constraining process.

Laramide Orogeny and Uplift

The Laramide orogeny succeeded the Western Interior Seaway ca. 84–80 Ma (Yonkee and Weil, 2015) and is believed to have partly contributed to the end of the Western Interior Seaway. Once inundated, the Western Interior Seaway region was kilometers above sea level. However, it remains unclear when the long-wavelength (>200 km) base elevation and the majority of the Laramide Province (Colorado Plateau and Wyoming) began rising to the present-day level (~2 km). The proposed timings range from the Late Cretaceous (Flowers et al., 2008; Liu and Gurnis, 2010; Flowers and Farley, 2012) to the mid-Cenozoic (Moucha et al., 2009). Whether dynamic topography contributed significantly to the present-day high topography also remains debated (Humphreys et al., 2003; Moucha et al., 2009; Liu and Gurnis, 2010; Becker et al., 2014). Forward landscape evolution simulations can directly test the effects of dynamic topography on the topographic evolution and so quantify the significance of dynamic topography in the pre-Cenozoic elevation in the Western Interior Seaway region.

Significant Laramide uplift events occurred in the western-middle continent ca. 80-40 Ma (Yonkee and Weil, 2015), overlapping the Western Interior Seaway both spatially and temporally. We suggest that localized Laramide uplift events would not change the overall simulated Western Interior Seaway sedimentation history over the Late Cretaceous. For the sedimentation history, uplifts of distributed Laramide ranges are unlikely to have been able to make major differences in the regional-scale sediment distribution, given their relatively small spatial scales. These uplifts could, instead, increase the amount of sedimentation via induced erosion in the localized uplifts and partly explain the insufficient sedimentation during 72-66 Ma in S2

(Fig. 9). Hence, it is justifiable to exclude the individual Laramide uplifts when considering the Western Interior Seaway sedimentation history in this study.

In the case of the regional-scale uplift of the Laramide Province, it can certainly have disturbed the large-scale sedimentation patterns. Indeed, the observed sedimentation ca. 72-66 Ma suggests some large-scale effects of Laramide uplifts on sedimentation in the Colorado Plateau and western Wyoming, where the observed amount is significantly smaller than that in the surrounding area. This period is at least 10 m.y. after the initiation of the Laramide orogeny (DeCelles, 2004), so its influence should already have become apparent. Here, the model results seem to imply that the effect of such regional-scale uplift should be weaker than that of contemporary dynamic subsidence prior to the Cenozoic. On one hand, this is because the combined effect of dynamic topography change and sedimentation already raised the regional topography to above sea level from 72 to 66 Ma (Fig. 8). On the other hand, additional topographic rise in the region since the beginning of the Laramide orogeny would have shut down sedimentation earlier and reduced the regional sediment accumulation, which would degrade the match to observations.

Because the magnitude of regional-scale pre-Cenozoic Laramide uplift likely was small, the initial elevation of the Laramide Province would have grown in the Late Cretaceous mainly due to dynamic topography and sedimentation combined. In S2, the elevation in this region is already above sea level at 66 Ma, so the sedimentation ends. The elevation gain after that could partly come from changes in dynamic topography, which can explain ~1 km of the observed ~2 km background elevation in the region according to DS2 (Liu and Gurnis, 2010). Hence, additional Laramide uplift of at least 1 km is required to raise the regional topography to the observed present elevation. Recent studies suggest that Cenozoic dynamic uplift within the western United States was mostly restricted to the Basin and Range Province (Becker et al., 2014; Zhou and Liu, 2019). If true, these results suggest that the 1 km of additional post-Western Interior Seaway uplift beyond the Basin and Range likely resulted from a buoyancy increase within the continental lithosphere (Humphreys et al., 2003; Jones et al., 2015; Schwartz et al., 2019).

CONCLUSION

In this study, we used forward landscape evolution simulations to test four tectonic scenarios for the formation of the Western Interior Seaway and investigated their associated surface manifestations with uncertainty tests on the parameters in landscape evolution. We show that foreland sediment can be a valid proxy for orogenic uplift models and that there must have been dynamic subsidence involved in the formation of Western Interior Seaway. We also show that the dynamic subsidence model with 1-kmscale magnitude and eastward migration can best explain the Western Interior Seaway sedimentation history. In particular, only such a model can reproduce the observed eastward-migrating depocenter and the intensity of sedimentation. This suggests that the dynamic subsidence causing the Western Interior Seaway was most likely due to regional-scale mantle downwelling associated with the sinking Farallon slab underneath the westward-moving North American plate. The landscape evolution simulation allowed us to further quantify the extent of impacts of the dynamic topography on surface processes. By comparing the predicted and observed sediment isopach thicknesses, we demonstrated that the migratory dynamic subsidence was the dominant control on the sedimentation pattern during 90-66 Ma, prior to which Sevier loading dominated. In addition, the landscape evolution simulation suggests that regional-scale uplift in the western United States during the Western Interior Seaway period was likely small, and the pre-Cenozoic elevation growth can be attributed to the effects of dynamic topography and sedimentation.

ACKNOWLEDGMENTS

The surface process code Badlands is available at https://github.com/badlands-model. We used the dynamic topography models provided at https://www.earthbyte.org. We thank Lon Abbott and Shaofeng Liu for their reviews, which greatly improved this manuscript. This research was partially supported by National Science Foundation grant EAR-1554554.

REFERENCES CITED

Artyushkov, E.V., 1992, Role of crustal stretching on subsidence of the continental crust: Tectonophysics, v. 215, p. 187–207, https://doi.org/10.1016/0040-1951(92)9 0081-G.

Becker, T.W., Faccenna, C., Humphreys, E.D., Lowry, A.R., and Miller, M.S., 2014, Static and dynamic support of western United States topography: Earth and Planetary Science Letters, v. 402, p. 234–246, https://doi .org/10.1016/j.epsl.2013.10.012.

Bond, G., 1976, Evidence for continental subsidence in North America during the Late Cretaceous global submergence: Geology, v. 4, p. 557–560, https://doi .org/10.1130/0091-7613(1976)4<557:EFCSIN>2.0 .CO;2.

Braun, J., 2010, The many surface expressions of mantle dynamics: Nature Geoscience, v. 3, p. 825–833, https://doi.org/10.1038/ngeo1020.

Chang, C., and Liu, L., 2019, Distinct responses of intraplate sedimentation to different subsidence mechanisms: Insights from forward landscape evolution simulations: Journal of Geophysical Research–Earth Surface, v. 124, p. 1139–1159, https://doi.org/10.1029/2018JF004905.

Chen, A., Darbon, J.Ô., and Morel, J.M., 2014, Landscape evolution models: A review of their fundamental

- equations: Geomorphology, v. 219, p. 68–86, https://doi.org/10.1016/j.geomorph.2014.04.037.
- DeCelles, P.G., 2004, Late Jurassic to Eocene evolution of the Cordilleran thrust belt and foreland basin system, western U.S.: American Journal of Science, v. 304, p. 105–168, https://doi.org/10.2475/ajs.304.2.105.
- Dietrich, W.E., Reiss, R., Hsu, M., and Montgomery, D.R., 1995, A process-based model for colluvial soil depth and shallow landsliding using digital elevation data: Hydrological Processes, v. 9, p. 383–400, https://doi.org/10.1002/hyp.3360090311.
- Ding, X., Salles, T., Flament, N., Mallard, C., and Rey, P.F., 2019, Drainage and sedimentary responses to dynamic topography: Geophysical Research Letters, v. 46, p. 14385–14394, https://doi. org/10.1029/2019GL084400.
- Fan, M., and Carrapa, B., 2014, Late Cretaceous-early Eocene Laramide uplift, exhumation, and basin subsidence in Wyoming: Crustal responses to flat slab subduction: Tectonics, v. 33, p. 509–529, https://doi .org/10.1002/2012TC003221.
- Flament, N., Gurnis, M., and Müller, R.D., 2013, A review of observations and models of dynamic topography: Lithosphere, v. 5, p. 189–210, https://doi.org/10.1130/ 1.245.1.
- Flowers, R.M., and Farley, K.A., 2012, Apatite ⁴He/³He and (U-Th): He evidence for an ancient Grand Canyon: Science, v. 338, p. 1616–1619, https://doi.org/10.1126/science.1229390.
- Flowers, R.M., Wernicke, B.P., and Farley, K.A., 2008, Unroofing, incision, and uplift history of the southwestern Colorado Plateau from apatite (U-Th)/He thermochronometry: Geological Society of America Bulletin, v. 120, p. 571–587, https://doi.org/10.1130/B26231.1.
- Gurnis, M., 1993, Continents driven by dynamic topography above subducting slabs: Nature, v. 364, p. 589–593, https://doi.org/10.1038/364589a0.
- Gurnis, M., Müller, R.D., and Moresi, L., 1998, Dynamics of Cretaceous to the present vertical motion of Australia and the origin of the Australian-Antarctic discordance: Science, v. 279, p. 1499–1504, https://doi.org/10.1126/ science.279.5356.1499.
- Haq, N., Hardenbol, J. and Vail, P., 1987, Chronology of fluctuating sea levels since the Triassic: Science, v. 235, p. 1156–1167, https://doi.org/science.235.4793.1156.
- Heine, C., Dietmar Müller, R., Steinberger, B., and Torsvik, T.H., 2008, Subsidence in intracontinental basins due to dynamic topography: Physics of the Earth and Planetary Interiors, v. 171, p. 252–264, https://doi.org/10.1016/j.pepi.2008.05.008.
- Heller, P.L., and Liu, L., 2016, Dynamic topography and vertical motion of the U.S. Rocky Mountain region prior to and during the Laramide orogeny: Geological Society of America Bulletin, v. 128, p. 973–988, https://doi.org/10.1130/B31431.1.
- Humphreys, E., Hessler, E., Dueker, K., Farmer, G.L., Erslev, E., and Atwater, T., 2003, How Laramide-age hydration of North American lithosphere by the Farallon slab controlled subsequent activity in the western United States: International Geology Review, v. 45, p. 575–595, https://doi.org/10.2747/0020-6814.45.7.575.
- Jones, C.H., Mahan, K.H., Butcher, L.A., Levandowski, W.B., and Farmer, G.L., 2015, Continental uplift through crustal hydration: Geology, v. 43, p. 355–358, https://doi.org/10.1130/G36509.1.
- Lague, D., Hovius, N., and Davy, P., 2005, Discharge, discharge variability, and the bedrock channel profile: Journal of Geophysical Research–Earth Surface, v. 110, F04006, https://doi.org/10.1029/2004JF000259.
- Leary, R., Decelles, P., Gehrels, G., and Morriss, M., 2015, Fluvial deposition during transition from flexural to dynamic subsidence in the Cordilleran foreland basin: Ericson Formation, western Wyoming, USA: Basin Research, v. 27, p. 495–516, https://doi.org/10.1111/ bre.12085.

- Liu, L., 2015, The ups and downs of North America: Evaluating the role of mantle dynamic topography since the Mesozoic: Reviews of Geophysics, v. 53, p. 1022–1049, https://doi.org/10.1002/2015RG000489.
- Liu, L., and Gurnis, M., 2010, Dynamic subsidence and uplift of the Colorado Plateau: Geology, v. 38, p. 663–666, https://doi.org/10.1130/G30624.1.
- Liu, L., Spasojević, S., and Gurnis, M., 2008, Reconstructing Farallon plate subduction beneath North America back to the Late Cretaceous: Science, v. 322, p. 934–938, https://doi.org/10.1126/science.1162921.
- Liu, L., Gurnis, M., Seton, M., Saleeby, J., Müller, R.D., and Jackson, J.M., 2010, The role of oceanic plateau subduction in the Laramide orogeny: Nature Geoscience, v. 3, p. 353–357, https://doi.org/10.1038/ngeo829.
- Liu, S., and Nummedal, D., 2004, Late Cretaceous subsidence in Wyoming: Quantifying the dynamic component: Geology, v. 32, p. 397–400, https://doi .org/10.1130/G20318.1.
- Liu, S., Nummedal, D., Yin, P.G., and Luo, H.J., 2005, Linkage of Sevier thrusting episodes and Late Cretaceous foreland basin megasequences across southern Wyoming (USA): Basin Research, v. 17, p. 487–506, https://doi.org/10.1111/j.1365-2117.2005.00277.x.
- Liu, S., Nummedal, D., and Liu, L., 2011, Migration of dynamic subsidence across the Late Cretaceous United States Western Interior Basin in response to Farallon plate subduction: Geology, v. 39, p. 555–558, https:// doi.org/10.1130/G31692.1.
- Liu, S., Nummedal, D., and Gurnis, M., 2014, Dynamic versus flexural controls of Late Cretaceous Western Interior Basin, USA: Earth and Planetary Science Letters, v. 389, p. 221–229, https://doi.org/10.1016/ j.epsl.2014.01.006.
- Milanovsky, E.E., 1992, Aulacogens and aulacogeosynclines: Regularities in setting and evolution: Tectonophysics, v. 215, p. 55–68, https://doi.org/10.1016/0040 -1951(92)90074-G.
- Mitrovica, J.X., Beaumont, C., and Jarvis, G.T., 1989, Tilting of continental interiors by the dynamical effects of subduction: Tectonics, v. 8, p. 1079–1094, https://doi .org/10.1029/TC008i005p01079.
- Moucha, R., Forte, A.M., Rowley, D.B., Mitrovica, J.X., Simmons, N.A., and Grand, S.P., 2009, Deep mantle forces and the uplift of the Colorado Plateau: Geophysical Research Letters, L19310, https://doi .org/10.1029/2009GL039778.
- Müller, R.D., Flament, N., Matthews, K.J., Williams, S.E., and Gurnis, M., 2016, Formation of Australian continental margin highlands driven by plate-mantle interaction: Earth and Planetary Science Letters, v. 441, p. 60–70, https://doi.org/10.1016/j.epsl.2016.02.025.
- Müller, R.D., Hassan, R., Gurnis, M., Flament, N., and Williams, S.E., 2018. Dynamic topography of passive continental margins and their hinterlands since the Cretaceous: Gondwana Research, v. 53, p. 225–251, https://doi.org/10.1016/j.gr.2017.04.028.
- O'Callaghan, J.F., and Mark, D.M., 1984, The extraction of ordered vector drainage networks from elevation data: Computer Vision Graphics and Image Processing, v. 28, p. 323–344, https://doi.org/10.1016/S0734-189X(84)80011-0.
- Painter, C.S., and Carrapa, B., 2013, Flexural versus dynamic processes of subsidence in the North American Cordillera foreland basin: Geophysical Research Letters, v. 40, p. 4249–4253, https://doi.org/10.1002/grl.50831.
- Peltier, W.R., 2004, Global glacial isostasy and the surface of the ice-age Earth: The ICE-5G (VM2) model and GRACE: Annual Review of Earth and Planetary Sciences, v. 32, p. 111–149, https://doi.org/10.1146/ annurev.earth.32.082503.144359.
- Robinson Roberts, L.N., and Kirschbaum, M.A., 1995, Paleogeography of the Late Cretaceous of the Western Interior of Middle North America—Coal Distribution and Sediment Accumulation: U.S. Geological

- Survey Professional Paper 1561, 115 p., https://doi.org/10.3133/pp1561.
- Rubey, M., Brune, S., Heine, C., Davies, D.R., Williams, S.E., and Müller, R.D., 2017, Global patterns in Earth's dynamic topography since the Jurassic: The role of subducted slabs: Solid Earth, v. 8, p. 899–919, https://doi .org/10.5194/se-8-899-2017.
- Salles, T., 2016, Badlands: A parallel basin and landscape dynamics model: SoftwareX, v. 5, p. 195–202, https:// doi.org/10.1016/j.softx.2016.08.005.
- Salles, T., and Hardiman, L., 2016, Badlands: An opensource, flexible and parallel framework to study landscape dynamics: Computers & Geosciences, v. 91, p. 77–89, https://doi.org/10.1016/j.cageo.2016.03.011.
- Salles, T., Flament, N., and Müller, D., 2017, Influence of mantle flow on the drainage of eastern Australia since the Jurassic Period: Geochemistry Geophysics Geosystems, v. 18, p. 280–305, https://doi.org/10.1002/2016GC006617.
- Salles, T., Ding, X., and Brocard, G., 2018, pyBadlands: A framework to simulate sediment transport, landscape dynamics and basin stratigraphic evolution through space and time: PLoS One, v. 13, p. 1–24, https://doi .org/10.1371/journal.pone.0195557.
- Schwartz, T.M., Methner, K., Mulch, A., Graham, S.A., and Chamberlain, C.P., 2019, Paleogene topographic and climatic evolution of the Northern Rocky Mountains from integrated sedimentary and isotopic data: Geological Society of America Bulletin, v. 131, p. 1203–1223, https://doi.org/10.1130/B32068.1.
- Smith, A.G., Smith, D.G., and Funnell, B.M., 1994, Atlas of Mesozoic and Cenozoic Coastlines: New York, Cambridge University Press, 99 p.
- Spasojevic, S., Liu, L., and Gurnis, M., 2009, Adjoint models of mantle convection with seismic, plate motion, and stratigraphic constraints: North America since the Late Cretaceous: Geochemistry Geophysics Geosystems, v. 10, Q05W02, https://doi .org/10.1029/2008GC002345.
- Tucker, G.E., and Hancock, G.R., 2010, Modelling landscape evolution: Earth Surface Processes and Landforms, v. 35, p. 28–50, https://doi.org/10.1002/esp.1952.
- Tufano, B.C., and Pietras, J.T., 2017, Coupled flexuraldynamic subsidence modeling approach for retroforeland basins: Example from the Western Canada Sedimentary Basin: Geological Society of America Bulletin, v. 129, p. 1622–1635, https://doi.org/10.1130/ B31646.1.
- Whipple, K.X., and Tucker, G.E., 1999, Dynamics of the stream-power river incision model: Implications for height limits of mountain ranges, landscape response timescales, and research needs: Journal of Geophysical Research–Solid Earth, v. 104, p. 17661–17674, https:// doi.org/10.1029/1999JB900120.
- Wickert, A.D., 2016, Open-source modular solutions for flexural isostasy: GFlex v1.0: Geoscientific Model Development, v. 9, p. 997–1017, https://doi.org/10.5194/ gmd-9-997-2016.
- Yonkee, W.A., and Weil, A.B., 2015, Tectonic evolution of the Sevier and Laramide belts within the North American Cordillera orogenic system: Earth-Science Reviews, v. 150, p. 531–593, https://doi.org/10.1016/ j.earscirev.2015.08.001.
- Zhou, Q., and Liu, L., 2019, Topographic evolution of the western United States since the early Miocene: Earth and Planetary Science Letters, v. 514, p. 1–12, https:// doi.org/10.1016/j.epsl.2019.02.029.

SCIENCE EDITOR: WENJIAO XIAO ASSOCIATE EDITOR: XIXI ZHAO

Manuscript Received 5 February 2020 Revised Manuscript Received 29 March 2020 Manuscript Accepted 1 May 2020

Printed in the USA